Analysis and Modeling of UAV Power System Architectures

Alastair P. Thurlbeck, *Student Member, IEEE,* Yue Cao, *Member, IEEE*
School of Electrical Engineering and Computer Science
Oregon State University, Corvallis, OR 97331
thurlbea@oregonstate.edu, yue.cao@oregonstate.edu

***Abstract*—This paper establishes a comprehensive modeling framework for vertical take-off and landing unmanned aerial vehicles (VTOL UAVs). An example UAV platform is designed to demonstrate applications of the model. Power system architectures are compared based on power losses, craft mass and flight-time. A realistic mission profile is used to examine power system losses and required input energy over various flight stages. Simulation shows a hybrid fuel cell stack and battery architecture allows for a heavier craft payload or increased maximum flight-time compared to conventional battery supplied power systems. Optimization plots demonstrate the usefulness of the model in UAV power system design.**

Keywords—Unmanned Aerial Vehicle, UAV, inverter, PMSM, SPM, permanent magnet, dc bus, flight-time, power system, modeling

I. INTRODUCTION

Unmanned Aerial Vehicles (UAVs) have dramatically increased in prominence in recent years. Whilst the military applications of fixed wing UAVs are well established [1], it is now the vertical take-off and landing (VTOL) UAV that shows the most promise for future commercial applications. The VTOL UAV offers inherent advantages such as scalability, a compact footprint and little required infrastructure. Recently, there has been a large increase in the use of lightweight DC-powered VTOL UAVs (colloquially known as “drones”). Such drones have been successfully deployed in new commercial applications such as cinematography, entertainment and industrial inspections. Recent developments in control algorithms, improved redundancy and increased flight-time have helped to alleviate safety concerns and range limitations. Such advances may soon allow for VTOL UAV deployment in larger scale commercial applications such as package delivery [2] - [4] or even passenger vehicles [5], [6].

Alongside research in more electric aircraft (MEA), power system design for UAVs provides a means to investigate novel architectures, control strategies and system components relevant to future passenger aircraft developments. The UAV can serve as a scalable testbed for power systems without the prohibitive costs or safety concerns of experimenting with large commercial aircraft.

As the power rating of UAVs is increased, the efficiency, responsiveness and redundancy of the UAV power system becomes critical. This paper will focus on higher power, AC motor propelled VTOL UAVs, better suited to serve future commercial applications. Whilst higher power may be the main driving factor in the design of such a UAV, its redundancy, noise, and adherence to regulatory requirements are also critical.

This paper first considers the individual elements of UAV power systems, including the sources, distribution, power converters, propulsion motors and control requirements. Three example power system architectures are introduced for detailed analysis using the model. A static or averaged model is developed for each element of the power system. Elements are then cascaded together to form a complete power system model according to the desired system architecture. Dynamometer testing using a permanent magnet syncronous motor (PMSM) and DC-AC inverter is used to experimentally validate the modeling aproach. An example 15 kg, four propeller VTOL UAV is designed to provide a realistic use case for the model.

Applications of the model to the example UAV are then presented. Simulations are used to consider the power losses and parameter optimization of the previously introduced power system architectures. Although transient behaviour is not modeled in this paper, static models allow for simulation over relatively slow timescales. Thus a realistic flight mission profile is used to test the response of each power system architecture to the varying power demands of ascending, descending, hovering and cruising. The maximum flight-time of each architecture is simulated over a wide sweep of energy storage capacity, demonstrating the effect of both system efficiency and storage specific energy (energy per unit mass).

II. UAV POWER SYSTEM OVERVIEW

A generic UAV power system architecture consists of the following elements: power sources, DC-DC converters, a DC bus (DC link), DC-AC inverters, and propulsion motors. For this paper auxiliary loads such as microcontrollers, control ICs and the communication system are negligible since their power consumption is insignificant compared to that of the propulsion motors.

In architecture 1 of Fig. 1, a DC-DC converter at the output of the battery allows for a fixed DC bus voltage. A fixed bus voltage allows the motors to be driven at their most efficient operating point. Increasing bus voltage also reduces conduction losses in the distribution wires between the battery and inverters, resulting in smaller diameter and therefore lighter wiring. However, the DC-DC converter itself imposes extra power losses, weight, size and cost. For a VTOL UAV, this increase in mass causes a constant increase in required craft thrust and thus craft input power and energy. Thus this paper

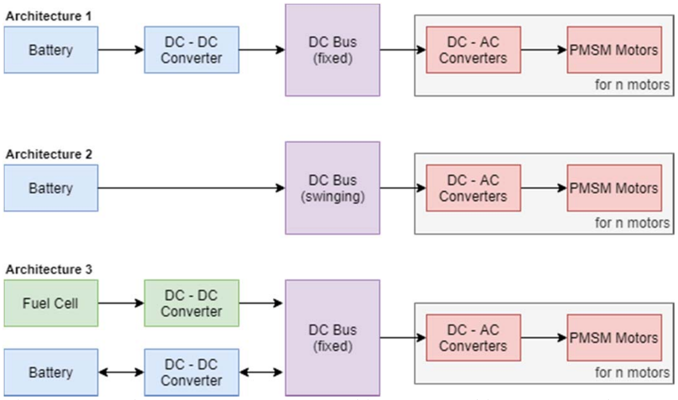

Fig. 1. Example UAV power system architecures. Architectures 1 and 2 use a battery as the primary energy source. In architecture 1 the battery voltage is boosted to a fixed DC bus voltage, whereas in architecture 2 the DC bus voltage is the varying battery voltage. Architecture 3 is a hybrid design in which a fuel cell stack is the primary energy source with a small battery as auxiliary storage.

will investigate the net impact of DC-DC converter inclusion with regard to input energy and flight-time.

In architecture 2 of Fig. 1, the DC-DC converter is omitted and the battery supplies the DC-AC inverters with a voltage that varies with battery state of charge (SOC) and load current. i.e. the DC bus voltage is the battery terminal voltage.

There is significant interest in hybrid powered systems utilizing a combination of batteries, fuel cells, solar cells or supercapacitors. The high specific energy of a hydrogen fuel cell makes it an ideal energy source for VTOL UAVs. However, modeling of a fuel cell powered UAV in [7] concluded that the transient response of a UAV would be significantly limited by the inherent time delay of the fuel cell. Thus architecture 3 shows a hybrid battery / fuel cell system. The battery can respond to fast load dynamics and peak power demands whilst a fuel cell stack provides the majority of power during cruising. A small battery can be used, which is recharged from the fuel cell during periods of reduced load demand. The hybrid system also offers improved redundancy, although UAV specific fuel cell stacks are expensive and not in widespread use.

Brushless DC (BLDC) motors are often chosen to power small VTOL UAV's. However as the aircraft size increases, permanent magnet AC (PMAC) motors offer reduced torque ripple and higher power density [8]. A lower cost alternative to permanent magnet motors are asynchronous induction machines (IM). Whilst induction machines are cheaper than PM machines, they are inherently less efficient and less compact [9]. They are thus less suited to UAV propulsion, where high power density and efficiency is required. For brevity, only PMAC motors are considered in this paper. The PMAC motors modelled are surface mounted permanent magnet (SPM) machines, though they are referred to more generally as permanent magnet synchronous machines (PMSM) in the remainder of this paper.

The remaining elements of the UAV power system are the DC-DC and DC-AC converters. DC-DC converters are optional and allow conversion from the battery or fuel cell voltage to a fixed DC bus voltage as in architecures 1 and 3. In architecture 3 a bidirectional converter such as the half bridge is required to charge the battery from the higher DC bus voltage. A DC-AC inverter is required to drive the PMSM motors with three phase AC from the DC bus. Various control schemes and modulation techniques may be applied to the inverter. In this paper, field-orientated control (FOC) and space vector modulation (SVM) are assumed.

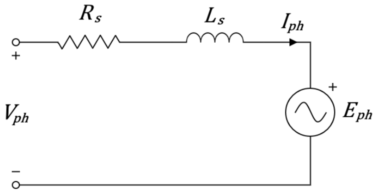

Fig. 2. Per phase equivalent circuit for a permanent magnet synchronous motor.

III. UAV Component and System Modeling

A. *PMSM Motors (Surface Mounted)*

Fig. 2 shows the single phase equivalent circuit model used for the surface mount PMSM motors. Stator resistance, R_s, and syncronous inductance, L_s, were measured experimentally. Phasor analysis in the *d*-*q* reference frame was used based on the method of [10], where the rotor magnet defines the reference, *d*-axis. The back EMF, $E_{ph(q)}$ is calculated as

$$E_{ph(q)} = k_e \cdot \omega_\mathrm{r} \tag{1}$$

where ω_r is the rotor speed and k_e (Vs/rad) is the back EMF constant, calculated from the manufacturers specified motor constant, K_v (rpm/V). No-load and electromechanical torques are given by:

$$T_{nl} = \frac{P_{mech}}{\omega_r} \tag{2}$$

$$T_{em} = T_r + T_{nl} \tag{3}$$

where P_{mech} is the combined mechanical and core losses. P_{mech} is calculated from a quadratic curve fit of the experimentally measured P_{mech} against motor speed. T_r is the rotor or load torque applied to the motor from the propeller. With no field weakening, $I_{ph(d)} = 0$ and thus the phase current magnitude is calculated as

$$|I_{ph}| = I_{ph(q)} = \frac{T_{em}}{3 \cdot k_e}. \tag{4}$$

The *d* and *q* axis components and the magnitude of the phase voltage are given by:

$$V_{ph(d)} = -\omega_r \cdot polepairs \cdot L_s \cdot I_{ph(q)} \tag{5}$$

$$V_{ph(q)} = E_{ph(q)} + R_s \cdot I_{ph(q)} \tag{6}$$

$$|V_{ph}| = \sqrt{{V_{ph(d)}}^2 + {V_{ph(q)}}^2} \tag{7}$$

where $polepairs$ is the number of magnetic pole pairs in the motor and thus relates rotor to electrical frequency. Total power loss and input power are calculated as:

$$P_{losses} = 3 \cdot R_s \cdot \left|I_{ph}\right|^2 + P_{mech} \tag{8}$$

$$P_{in} = P_{losses} + T_r \cdot \omega_r \tag{9}$$

The modulation index, m_a is given by

$$m_a = \frac{2\sqrt{2} \cdot |V_{ph}|}{V_{bus}}. \tag{10}$$

B. DC-AC Inverters

The DC-AC inverter is a hex bridge topology using a number of MOSFETs in parallel in each phase leg, $nump$. The inverter uses FOC with SVM. The phase current referenced to a single MOSFET is then given by

$$I_{ph}{}' = I_{ph}/nump. \tag{11}$$

The phase angle, θ, was assumed to be 18.2°. The average switching current experienced by the MOSFET is the average of a half sinusoid:

$$I_{sw} = \frac{2\sqrt{2} \cdot I_{ph}{}'}{\pi}. \tag{12}$$

Switching voltage rise and fall times are estimated using the method of [11], in which the gate to drain capacitance, C_{GD}, is defined during two periods such that:

$$C_{GD1} = C_{GD}(V_{bus}) \tag{13}$$

$$C_{GD2} = C_{GD}(R_{DSon} \cdot I_{sw}) \tag{14}$$

Then the voltage rise and fall time, trv and tfv are given by:

$$trv1 = (V_{bus} - R_{DSon} \cdot I_{sw}) \cdot R_G \cdot \frac{C_{GD1}}{V_{miller}} \tag{15}$$

$$trv2 = (V_{bus} - R_{DSon} \cdot I_{sw}) \cdot R_G \cdot \frac{C_{GD2}}{V_{miller}} \tag{16}$$

$$tfv1 = (V_{bus} - R_{DSon} \cdot I_{sw}) \cdot R_G \cdot \frac{C_{GD1}}{(V_{dr} - V_{miller})} \tag{17}$$

$$tfv2 = (V_{bus} - R_{DSon} \cdot I_{sw}) \cdot R_G \cdot \frac{C_{GD2}}{(V_{dr} - V_{miller})} \tag{18}$$

$$trv = \frac{trv1 + trv2}{2} \tag{19}$$

$$tfv = \frac{tfv1 + tfv2}{2} \tag{20}$$

where R_G is the sum of internal and external gate resistances, V_{dr} is the applied gate drive voltage and V_{miller} is the gate plateau voltage. The current rise and fall times, tri and tfi are given by the MOSFET datasheet.

Switching losses in the MOSFET (q) and diode (d) are then calculated based on their respective turn on and turn off energies:

$$E_{on(q)} = V_{bus} \cdot I_{sw} \cdot \frac{tri + tfv}{2} + Q_{rr} \cdot V_{bus} \tag{21}$$

$$E_{off(q)} = V_{bus} \cdot I_{sw} \cdot \frac{trv + tfi}{2} \tag{22}$$

$$E_{on(d)} = \frac{1}{4} \cdot Q_{rr} \cdot V_{bus} \tag{23}$$

where Q_{rr} is the body diode reverse recovery charge. Average and rms MOSFET and body diode currents were calculated according to [12, Appendix I], assuming Null = V0 switching. Then the MOSFET and body diode conduction losses are given by:

$$P_{on(q)} = I_{q(rms)}^2 \cdot R_{DSon} \tag{24}$$

$$P_{on(d)} = I_{d(ave)} \cdot V_f + I_{d(rms)}^2 \cdot R_{diode} \tag{25}$$

where R_{DSon} is the on resistance of the MOSFET, V_f the forward voltage drop of the body diode and R_{diode} its on state resistance. Switching losses are given by:

$$P_{sw(q)} = \left(E_{on(q)} + E_{off(q)}\right) \cdot \frac{f_{sw}}{2} \tag{26}$$

$$P_{sw(d)} = E_{off(d)} \cdot \frac{f_{sw}}{2} \tag{27}$$

where f_{sw} is the switching frequency of the inverter. Total inverter losses, input power and input current are given by:

$$P_{losses} = 6 \cdot nump\left(P_{sw(q)} + P_{sw(d)} + P_{on(q)} + P_{on(d)}\right) \tag{28}$$

$$P_{in} = P_{losses} + P_{out} \tag{29}$$

$$I_{in} = \frac{P_{in}}{V_{bus}} \tag{30}$$

C. DC-DC Converters (Boost and Half-Bridge)

Using an averaged converter model, the required average and rms MOSFET (q), inductor (L) and diode (d) currents for boost mode operation are calculated as:

$$I_{q(rms)} = \frac{I_{in}}{nump} \cdot \sqrt{(D)} \tag{31}$$

$$I_{L(rms)} = I_{in} \tag{32}$$

$$I_{d(rms)} = I_{in} \cdot \sqrt{(1 - D)} \tag{33}$$

$$I_{d(ave)} = I_{in} \cdot (1 - D) \tag{34}$$

where I_{in} is defined as the current flowing into the converter from the battery or fuel cell and $nump$ is the number of MOSFETs in parallel. The average and rms currents for the half-bridge converter operating in buck mode are calculated as:

$$I_{q(rms)} = \frac{I_{out}}{nump} \cdot \sqrt{(D)} \tag{35}$$

$$I_{L(rms)} = I_{out} \tag{36}$$

$$I_{d(rms)} = I_{out} \cdot \sqrt{(1 - D)} \tag{37}$$

$$I_{d(ave)} = I_{out} \cdot (1 - D) \tag{38}$$

where I_{out} is defined as the current flowing out of the converter to the battery. The inductor conduction loss is given by:

$$P_{on(L)} = I_{L(rms)}^2 \cdot DCR \tag{39}$$

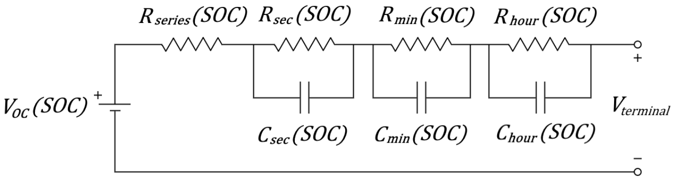

Fig. 3. Dynamic battery model from [13]. V, R and C elements are all functions of state of charge (SOC). For static simulation, capacitive elements are ignored and the resistivie elements summed together.

MOSFET and diode switching and conduction losses are calculated using the same method as for the DC-AC inverter, however the MOSFET body diode is now neglected.

D. Lithium-Ion Battery

The battery can be modelled dynamically using a three-time constant Randles' equivalent circuit [13] as shown in Fig. 3. Logarithmic-polynomial interpolation equations (40) with coefficients from [13, Table II] are used to calculate the equivalent circuit elements as a function of battery state of charge (SOC):

$$\ln(V, R, C) = \sum_{k=0}^{6} a_k \cdot ln^k(SOC) \tag{40}$$

For static simulation, capacitive elements are ignored and the resistances can then be summed together into an equivalent resistance, R_{static}. Since the cell tested in [13] had a specified maximum discharge rate of 1C, the resistance was decreased by a factor of 5 in order to support the required discharge rates of 5C or higher. The accuracy of the model should be increased by applying this equivalent circuit approach to an application specific high discharge rate Li-Po battery pack.

E. Fuel Cell Stack

Fig. 4 shows the generic fuel cell model. The modeling approach is described in [14] and allows all the necessary model parameters to be extracted from the manufacturer's polarization curve. The simplified model includes the activation losses, ohmic losses and a delay to represent stack settling time. For static simulation the delay is ignored. The polarization curve of the Horizon 3000W PEM Fuel Cell was used to generate realistic model parameters.

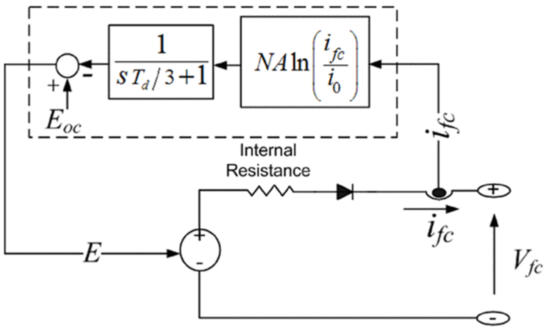

Fig. 4. Generic fuel cell model from [14], including activation and ohmic losses. The low pass transfer function representing the stack settling time is removed for static simulation.

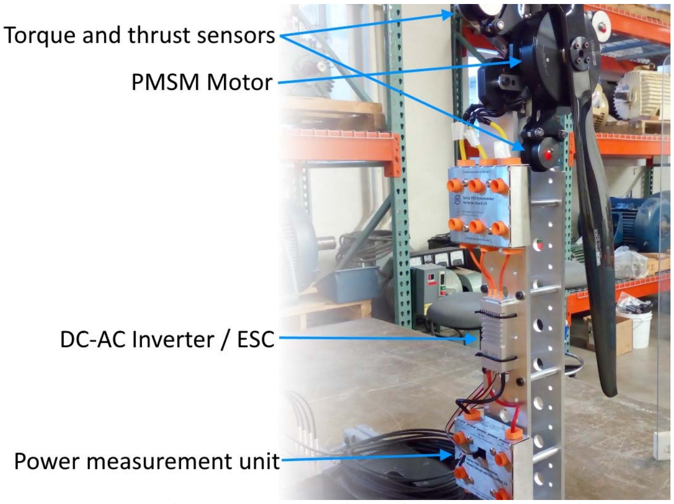

Fig. 5. Experimental setup consisting of a surface mount PMSM driven by a DC-AC inverter or electronic speed controller (ESC). A propeller applies a realistic load torque to the motor.

IV. EXPERIMENTAL VALIDATION

Fig. 5 shows the experimental system consisting of a PMSM motor (T-Motor U10II KV100) driven by an FOC based ESC / DC-AC inverter (T-Motor Alpha 80A HV). An RC Benchmark Dynamometer was used to measure output thrust, torque, speed and power as well as the input power to the DC-AC inverter. A no-load test was used to experimentally determine the motor's mechanical losses. The MOSFET arrangement and model parameters were determined for the DC-AC inverter, whilst equivalent circuit parameters were obtained for the motor. Two propellers (T-Motor G28x9.2 and G30x10.5) were used to apply realistic load torques to the motor. The motor speed was slowly swept from zero to its rated condition to minimize torque due to acceleration. Combined power loss and efficiency from inverter input to motor shaft were measured. The model was then swept over the same torque and speed values to compare the calculated losses and efficiency to the experimental results.

Fig. 6. Model calculated losses compared to the experimentally measured losses. The experiment was carried out with two sizes of propeller. With the G28x9.2 propeller, the motor was swept to its rated speed whilst with the G30x10.5 propeller, the motor was swept to its rated current.

The recorded torque, speed and thrust values were also used in the mission profile simulations to realistically map required thrust to motor torque and speed. Fig. 6 compares the experimentally measured losses to the model calculated losses. The model is reasonably close to the experimental results over the entire speed range. However, losses are generally overestimated, particularly at low speed or thrust values. The model is deemed to be sufficiently accurate for power system design purposes and analysis.

V. MODEL APPLICATION TO AN EXAMPLE SYSTEM

A. Model Parameters and Configuration

An example four propeller VTOL UAV was designed to provide a sample application for the modeling framework. The system components and mass are outlined in Table I. The UAV was designed for a maximum continuous thrust of 24 kgf which corresponds to 1.6 times the maximum loaded craft mass of 15 kg. Assuming the total mass is held constant, payload mass varies between 2.35 and 4.04 kg depending on the power system architecture. The mass of the propellers, motors and DC-AC inverters were specified by the manufacturer. Battery mass was calculated based on 3.7 V, 2200 mAh Lithium Polymer (Li-Po) cells in a 12 series, 9 parallel configuration. The mass was then calculated from the capacity divided by the specific energy for a representative UAV Li-Po battery pack. The fuel cell stack mass is calculated as the required energy capacity divided by the specific energy of a similiarly sized UAV specific fuel cell power module.

Wiring losses are calculated based on the mass per unit length of AWG10, AWG12 and AWG14 wires. For simplicity, wiring losses are calculated within the battery, fuel cell, boost and DC-AC inverter models. Wiring loss is calculated as the I^2R loss based on the output current, wire size, wire quantity and wiring length following the subsystem. Wiring losses are accounted for in the input power required by each subsystem, however are not included in each subsystem's power loss and efficiency calculation. Instead wiring losses are summed together to form a combined figure for system wiring loss.

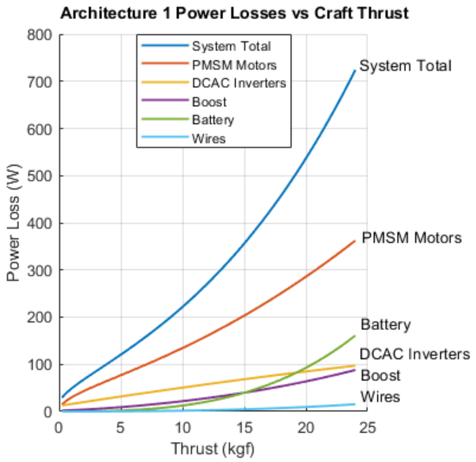

Fig. 7. Power loss breakdown for Architecture 1. Thrust is converted to motor torque and speed using the experimental data for the G28x9.2 propeller.

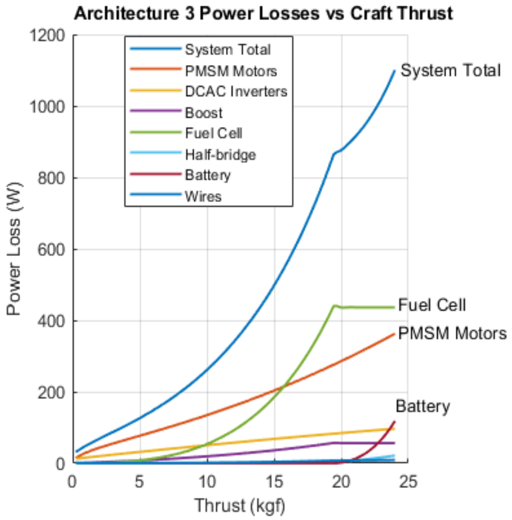

Fig. 8. Power loss breakdown for Architecture 3. Thrust is converted to motor torque and speed using the experimental data for the G28x9.2 propeller.

B. Static System Loss Breakdown

The model can be configured to implement the three architecures of of Fig. 1. A simple application of the model is to calculate and compare the losses of each of the power system components over the output thrust of the craft. Fig. 7 shows the breakdown of power losses for architecture 1 whilst Fig. 8 shows the power losses of architecture 3. In architecture 1, the PMSM motors dominate the losses, though the battery and boost losses become increasingly signficant at higher thrust. The boost converter losses are not present in architecture 2, however the rest of the losses are comparable. In architecture 3 the losses are considerably higher over the

TABLE I.
VTOL UAV COMPONENT MASS DETERMINATION

Component	**Data Source for Mass Calculation**	**Arch 1 Mass (kg)**	**Arch 2 Mass (kg)**	**Arch 3 Mass (kg)**
Propellers	T-Motor G28x9.2, specified mass.	0.392	0.392	0.392
Motors	T-Motor U10II KV100, specified mass.	1.660	1.660	1.660
Inverters (ESCs)	T-Motor Alpha 80A HV, specified mass.	0.440	0.440	0.440
Battery Pack	Tattu 10000mAh 6s 25C Lipo, specific energy, Wh/kg,	5.543	5.543	0.616
Fuel Cell Stack	Inteligent Energy UAV FCPM Brochure, specific energy, Wh/kg at 1100Wh capacity.	-	-	3.037
DC-DC Converters	US Drive EETT Roadmap, power electronics 2020 target power density, kW/kg.	1.417	-	1.620
Frame + Wiring	Estimation, approx 20% of 15kg designed mass.	3.000	3.000	3
Aux Electronics	Estimation	0.200	0.200	0.200
	Unloaded Craft Total (kg)	12.65	11.24	10.96

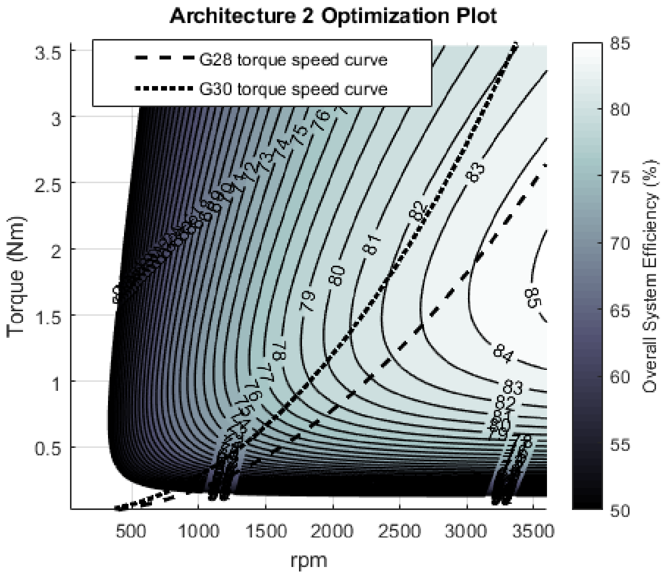

Fig. 9. Architecture 2 optimization plot over motor torque and rpm. White curves show actual relationship between torque and rpm for the two tested propellers.

entire thrust range of the craft. This is driven largely by the fuel cell losses. Beyond 19 kgf the fuel cell loss remains constant and the battery loss becomes significant. This is due to the current threshold for maximum fuel cell current being reached and the power management unit (PMU) demanding the extra current from the battery instead.

C. Power System Optimization

3D optimization plots can be generated by plotting the combined system efficency against two variables. Fig. 9 shows the relationship between motor torque and rpm and system efficiency for architecture 2. In reality, motor torque and rpm are not independent and vary with output thrust depending on the attached propeller. To illustrate this the torque-speed curves for the T-motor G28x9.2 and G30x10.5 propellers are also plotted. At high thrusts the system offers the best efficiency at higher rpm and lower torque (higher voltage, lower current).

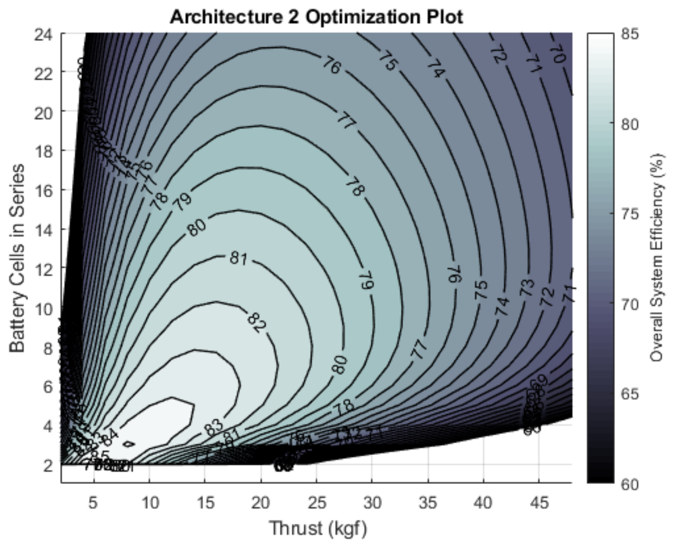

Fig. 10. Architecture 2 optimization plot over the number of battery cells in series and total output thrust. Hover thrust is defined as 15 kgf, cruising thrust is estimated at around 18 kgf and maximum continuous thrust is around 24 kgf.

Fig. 10 plots architecture 2 system efficiency against battery cells in series and craft thust. The number of battery cells in series effectively sets the DC bus voltage seen by the DC-AC inverter. The capacity of the battery pack is held constant by adjusting the number of cells in parallel. The optimization plot can thus guide battery pack design. At 15 kgf hover thrust, 7 cells in series would be optimal and at the designed maximum craft thrust of 24 kgf, 10 cells in series is optimum. However, at the theoretical maximum thrust demand of 31 kgf (based on rated motor current), 12 cells in series is optimum. This is as expected, as 12S is the manufacturers rated voltage for this motor.

D. Mission Profile Simulations

The mission profile of Fig. 11 was used to simulate each power system architecture over a realistic flight profile. Normalized thrust is defined as the ratio of actual thrust to craft mass. The total craft mass was designed to be 15 kg for all architectures, such that the required output power would not vary between architectures. The unloaded mass of architecture 1 was calculated to be 12.65kg, allowing a payload of 2.35 kg. Architecture 2 is identical except for the removal of the boost converter, giving an unloaded mass of 11.24kg and payload of 3.76 kg. Architecture 3 uses a fuel cell stack with equivalent capacity to the battery pack of Architectures 1 and 2. This allows for a significant weight saving due to the higher specific energy of the fuel cell by a factor of 1.83 compared to the Li-Po battery. Despite the addition of an auxiliary battery and a second DC-DC converter, Architecture 3 achieves an unloaded mass of around 10.96 kg, allowing for a payload of 4.04 kg (see Table I). If the payload was held constant at 2.35 kg, architectures 2 and 3 would be capable of a longer flight-time compared to architecture 1 as shown in subsection E.

Fig. 12 shows the results of mission profile simulations across the three architectures. Architecture 2 has the lowest losses and thus lowest required input energy over the entire mission profile. It is the most efficient, achieving an efficiency of around 83% for the majority of the flight. Architecture 1 has

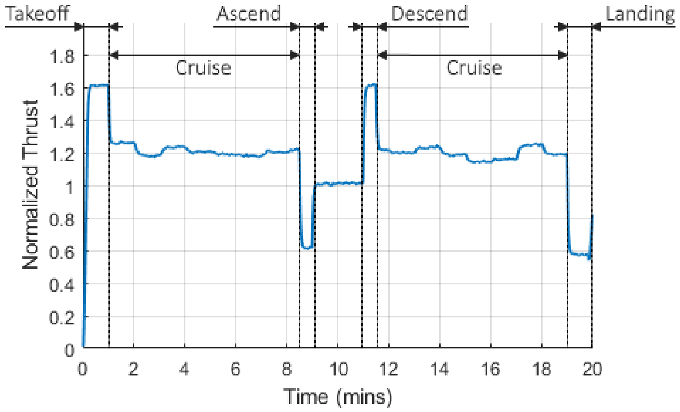

Fig. 11. Mission profile Simulation for a 20 minute representative flight. The total craft mass was held consant at 15 kg for each architecture, allowing architectures 2 and 3 to carry a heavier payload.

slightly increased losses compared to architecture 2 due to the addition of the boost converter. Architecture 3 was significantly less efficient than the other two architectures with much higher losses during the cruising or ascending stages of the mission profile. Primarily this is due to the modeled fuel cell stack having excessive losses. However, the hybrid design introduces additional losses when the battery is charged from the fuel cell during cruising. The fuel cell current is elevated to provide the extra charging current for the battery. This charging current then adds additional losses in the boost and half bridge converters, as charging is achieved via the DC bus.

E. Maximum Flight-Time Simulation

Fig. 13 shows the simulated maximum flight-time for each power system architecture. The simulation assumed a constant cruising thrust of 1.2 times the total craft mass. Total craft mass was calculated with a 2.3kg payload for all architectures. Mass was recalculated on each iteration based on the current battery or fuel cell capacity. Architecture 1 has the lowest maximum flight-time of 25.5 minutes at 3 kWh. Architecture 2 offers a considerable increase in maximum flight-time to 30 minutes at 2.7 kWh. This is due to reduced weight and efficiency savings when the boost converter stage is eliminated. Architecture 3 offers the highest maximum flight-time of around 32 minutes at 2.7 kWh. This is primarily due to the higher specific energy (1.83x) of the fuel cell stack compared to the liPo battery pack. However for shorter maximum flight-times, architecture 3 requires more energy capacity than architectures 1 and 2 due to its increased losses. Since

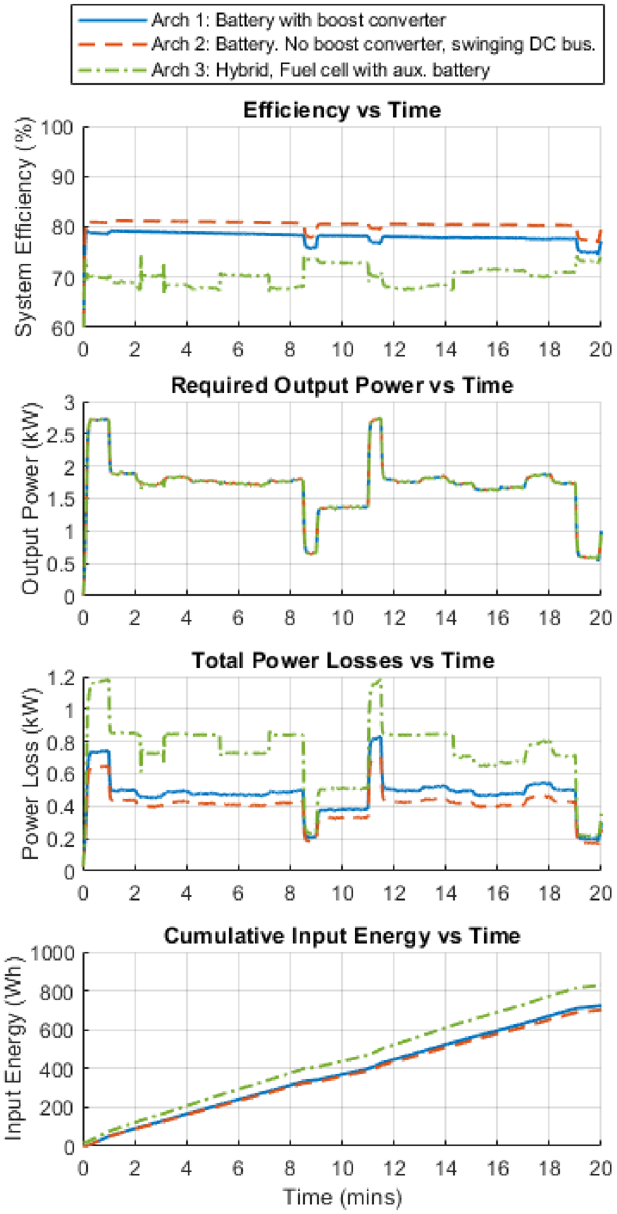

Fig. 12. Mission profile Simulation for a 20-minute representative flight. The total craft mass was held constant at 15 kg for each architecture, allowing architectures 2 and 3 to carry a heavier payload.

$$P_{out} \propto Thrust^{3/2}, \tag{41}$$

curves are aproximately of the form

$$t_{max} = \frac{c_1 \cdot E_{capacity}}{(c_2 \cdot E_{capacity}+c_3)^{3/2}}, \tag{42}$$

where $c_{1,2,3}$ are constants. However since the efficiency of the power system decreases rapidly at higher thrust levels, the simulated curves peak sooner and drop off faster.

VI. DISCUSSION

The mission profile, flight-time and static simulations all suggest architecture 2 to be more efficient than architectures 1 and 3. In addition, architecture 2's reduced mass allows for an increase in payload mass of 1.417 kg and a longer flight-time compared to architecture 1 (Fig. 11). However, due to the limited scope of this paper, architecture 1 assumed the use of a

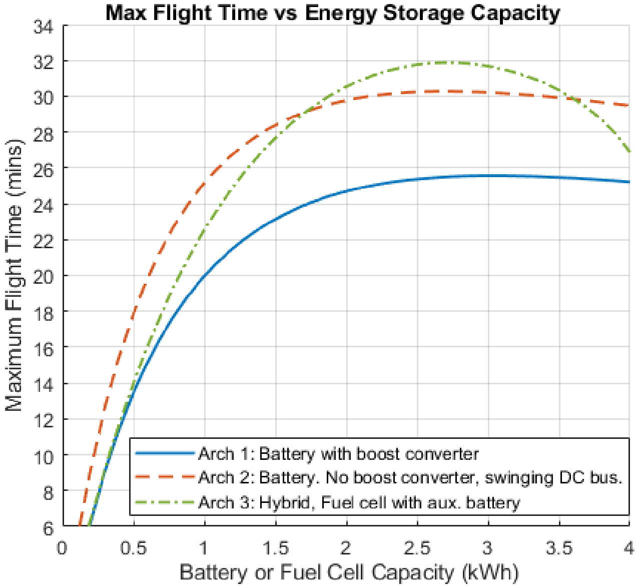

Fig. 13. Maximum flight-time against energy storage capacity for the three architectures. Simulation assumed a constant cruising thrust of 1.2x craft mass. Maximum flight-time was defined as the time at which the battery or fuel cell state of charge reached 20%.

boost converter to a fixed DC bus voltage. Reference [15] shows the efficiency of a PMSM motor and inverter can be improved by varying DC bus voltage with motor speed. Since phase voltage varys aproximately with motor speed, the bus voltage is increased as the motor speed is increased. Thus future modification of architecture 1 could consider using a universal step-up/step-down converter. An associated control scheme would implement varying DC bus voltage based on motor speed. It is expected that although this would offer an efficiency improvement, the required input power and energy of the craft would still be increased compared to architecture 2 due to the additional thrust requirement inherent to the VTOL UAV application.

The method used to calculate MOSFET turn on and turn off energy could be improved. Voltage rise and fall times are each calculated twice, once using the minimum value of gate-drain capacitance and once using the maximum value of gate-drain capacitance. The mean rise and fall time is then used. In reality, gate-drain capacitance is a function of drain-source voltage and the difference between the max and min values is often very large. For the MOSFET used in this paper, this range was between 27 pF and 800 pF. This rough aproximation likely gives rise to considerable inaccuracies in MOSFET switching loss calculation. An alternative approach is to experimentally measure turn on and turn off energies over I_{DS} and V_{DS}. However, this would limit the effectiveness of the model as a design tool, so using improved calculation methods is preferable for future work.

The battery model used experimental data for a cell with limited discharge capacity. Experimental data, gathered for a UAV specific high discharge rate battery pack for use with the logarithmic-polynomial interpolation method, is preferred.

The fuel cell model used in the example simulations used the polarization curve for the Horizon 3000W PEM Fuel Cell. However, this fuel cell stack was not designed for UAV applications and was prohibitely heavy. Instead the mass of the fuel cell used to calculate craft mass was based on the specific energy (Wh/kg) of a UAV specific fuel cell stack. To improve the realism of the simulations the model parameters and calculated mass should be based on the same fuel cell stack. This was not possible for this paper due to the limited availability of UAV specific fuel cell stacks.

VII. CONCLUSION

This paper presented a static modeling approach for VTOL UAV power systems. Hardware testing of a DC-AC inverter and PMSM motor allowed for validation of the proposed model. The modeled losses and efficiency were sufficiently accurate for the model to be used as an effective design tool, despite small differences between calculated and measured values. As the model tended to over-estimated power loss, this would lead to an overly conservative design of the UAV power system.

The paper then presented example applications of the model based on a realistic VTOL UAV design using three possible power system architectures. The model allowed for static simulation, mission profile simulation, maximum flight-time determination, energy storage sizing and parameter optimization studies. This modeling and simulation framework may be applied to any power system, serving as a critical design tool for future VTOL UAVs.

For the example UAV design, it was found that a hybrid power system (architecture 3) allowed for a craft mass reduction by using a higher density hydrogen fuel cell stack in place of lithium-ion batteries as the primary storage medium. This allowed for a heavier payload or increased maximum flight-time compared to a conventional battery supplied system (architecture 2).

It was found that using a boost converter to a fixed DC bus (architecture 1) decreased efficiency and maximum flight-time compared to the conventional approach of the DC bus voltage varying with battery voltage (architecture 2). In addition to increased losses, the DC-DC converter requires more craft thrust and thus an increase in craft output power. Thus even if a fixed DC bus delivers overall system efficiency improvements, the required input energy of the power system may still be higher.

REFERENCES

[1] Office of the Secretary of Defense, "U.S. Department of Defense Unmanned Aerial Vehicle Road Map 2005 - 2030," 2005. [Online]. Available: https://fas.org/irp/program/collect/uav_roadmap2005.pdf

[2] "DHL Parcelcopter." dpdhl.com. https://www.dpdhl.com/en/media-relations/specials/dhl-parcelcopter.html. (accessed Dec. 6, 2018).

[3] "Project Wing," x.company. https://x.company/projects/wing/. (accessed Dec. 6, 2018).

[4] "Amazon Prime Air," amazon.com. https://www.amazon.com/Amazon-Prime-Air/b?ie=UTF8&node=8037720011. (Accessed April. 18, 2019).

[5] "Kitty Hawk Aero," kittyhawk.aero. https://kittyhawk.aero/. (Accessed Dec. 6, 2018).

[6] "Ehang 184," ehang.com. http://www.ehang.com/ehang184/. (Accessed Dec. 6, 2018).

[7] M. Zhou and J. V. R. Prasad, "Transient characteristics of a fuel cell powered UAV propulsion system," in *Proc. Int. Conf. on Unmanned Aircraft Systems,* Atlanta, GA, USA, 2013, pp. 114-123.

[8] Z. Q. Zhu and D. Howe, "Electrical Machines and Drives for Electric, Hybrid, and Fuel Cell Vehicles," *Proceedings of the IEEE,* vol. 95, no. 4, pp. 746-765, Apr. 2007.

[9] J. G. Hayes and G. A. Goodarzi, "Introduction to Traction Machines," in *Electric Powertrain: energy systems, power electronics and drives for hybrid, electric and fuel cell vehicles*, Hoboken, NJ, John Wiley & Sons, 2018, ch. 6, pp. 161-177.

[10] J. G. Hayes and G. A. Goodarzi, "Per-Phase Analysis of SPM Machine," in *Electric Powertrain*, Hoboken, NJ, John Wiley & Sons, 2018, ch. 9.2, pp. 255-275.

[11] D. Graovac and M. Purschel, "MOSFET Power Losses Calculation Using the Data-Sheet Parameters," Infineon Application Note, 2006.

[12] P. J. P. Perruchoud and P. J. Pinewski, "Power losses for space vector modulation techniques," in *Proc. Power Electronics in Transportation,* Dearborn, MI, USA, 1996, pp. 167-173.

[13] Y. Cao, R. C. Kroeze and P. T. Krein, "Multi-timescale parametric electrical battery model for use in dynamic electric vehicle simulations," *IEEE Trans. Transport. Electrific.*, vol. 2, no. 4, pp. 432-442, Dec. 2016.

[14] S. N. M., O. Tremblay and L. Dessaint, "A generic fuel cell model for the simulation of fuel cell vehicles," in *Proc. IEEE Vehicle Power and Propulsion Conf.*, Dearborn, MI, USA, 2009, pp. 1722-1729.

[15] W. Deng, Y. Zhao and J. Wu, "Energy Efficiency Improvement via Bus Voltage Control of Inverter for Electric Vehicles," *IEEE Trans. Veh. Technol.,* vol. 66, no. 2, pp. 1063-1073, Apr. 2017.